Buckling of a monolayer of platelike particles trapped at a fluid-fluid interface

Suriya Prakash, Hugo Perrin, and Lorenzo Botto*

Department of Process & Energy, Faculty of Mechanical Engineering, Delft University of Technology, 2628CB Delft, The Netherlands

(Received 4 July 2023; accepted 14 December 2023; published 23 January 2024)

Particles trapped at a fluid-fluid interface by capillary forces can form a monolayer that jams and buckles when subject to uniaxial compression. Here we investigate experimentally the buckling mechanics of monolayers of millimeter-sized rigid plates trapped at a planar fluid-fluid interface subject to uniaxial compression in a Langmuir trough. We quantified the buckling wavelength and the associated force on the trough barriers as a function of the degree of compression. To explain the observed buckling wavelength and forces in the two-dimensional (2D) monolayer, we consider a simplified system composed of a linear chain of platelike particles. The chain system enables us to build a theoretical model which is then compared to the 2D monolayer data. Both the experiments and analytical model show that the wavelength of buckling of a monolayer of platelike particles is of the order of the particle size, a different scaling from the one usually reported for monolayers of spheres. A simple model of buckling surface pressure is also proposed, and an analysis of the effect of the bending rigidity resulting from a small overlap between nanosheet particles is presented. These results can be applied to the modeling of the interfacial rheology and buckling dynamics of interfacial layers of 2D nanomaterials.

DOI: 10.1103/PhysRevE.109.014801

I. INTRODUCTION

The buckling wavelength of monolayers of nearly spherical particles trapped at a fluid interface under compression has been studied with both realistic particles (Lycopodium spores, Chemigum (Eliokem)) [1] as well as model particles (glass beads, zirconium oxide beads) [2]. In these experiments the particles were spread at an air-water interface and the particle layer subject to uniaxial compression in a Langmuir trough. Both the buckling wavelength and the force on the barrier, proportional to the surface pressure [3], were measured. A mathematical model that treats the monolayer as a continuous elastic sheet captured the buckling wavelength measured in these experiments. The relation between the effective mechanical properties of the monolayer and the particle size was obtained by assuming an effective Young modulus $E \sim \gamma/d$, where γ is the surface tension of the bare fluid-fluid interface and d is the nominal sphere diameter [1]. According to this model, and in agreement with experimental results [1,2,4], the buckling wavelength of the monolayer scales as $\sim\sqrt{\ell_c d}$, where $\ell_c = \sqrt{\gamma/(\tilde{\rho} g)}$ is the capillary length, $\tilde{\rho}$ is the density difference between the two fluids across the interface, and g is the acceleration of gravity.

Compression experiments on buckling of interfacial monolayers of graphene oxide show a buckling wavelength in the range of 4–20 particle diameters, with an average wavelength of 7.6 particle diameters [5]. The continuum theory for spheres would give approximately 250 particle diameters, largely overestimating the observed wavelength. Given the large aspect ratio of graphene oxide sheets, applying models for spheres is questionable, and developing mathematical models specifically tailored to platelike particles is thus necessary. Deriving such models starting from experiments with nanoparticles, which are affected by uncontrolled variables such as polydispersity in size [6] and possibility of particle-particle overlap [7], is challenging. With a model experimental system, in which macroscopic particles of controlled shapes are used, one can investigate the associated interfacial mechanics without the complications of an actual nanoparticle system.

In this paper we study experimentally the uniaxial compression of a monolayer of millimeter-sized platelike particles trapped at a fluid-fluid interface by capillary forces. We start with observations of a two-dimensional (2D) monolayer of hexagonal particles at an air-water interface. We then consider a linear chain of square plates [one-dimensional (1D) system]. We develop a theory to explain the linear chain system which is then applied to the 2D particle monolayer. In our experiments the particles are not overlapping for most of the monolayer deformation. However, we use the 1D mathematical model to discuss possible implications of small overlaps between the particles in terms of an increased effective bending rigidity of the particle layer.

In our experiments the Bond number based on the weight of the particles is small [8], so the effect of downward distortion of the fluid interface owing to the weight of the particle (minus buoyancy) is relatively unimportant. However, as we will see, when in contact the particles can displace fluid by rotating around an axis parallel to the fluid interface. This results in a gravitational contribution to the interfacial mechanics. In the linear chain case, we are able to investigate the regime in which capillary forces are dominant over gravitational forces by density matching of the upper and lower fluids.

*Corresponding author: l.botto@tudelft.nl

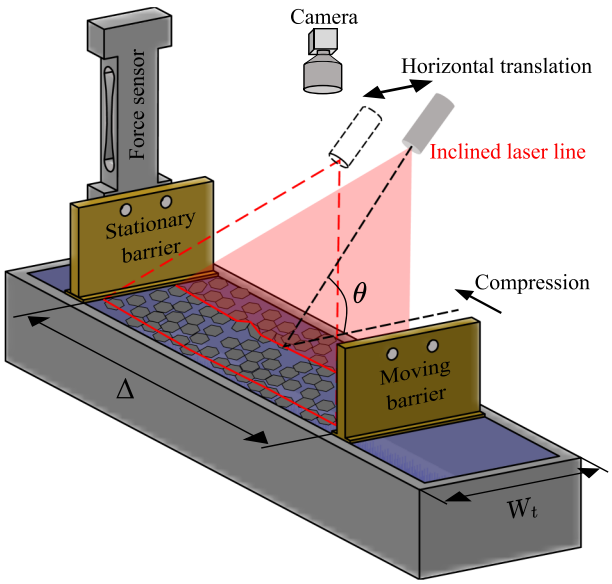

FIG. 1. Schematic of the experimental setup to measure surface pressure and topology of the interfacial monolayer of plates.

The motivation for the current work is to better understand the compression of 2D nanomaterials at fluid-fluid interfaces. Two-dimensional nanomaterials, of which the most discussed are graphene and graphene oxide, can take the form of a colloidal dispersion of nanometrically thin platelike particles of large aspect ratios [9,10]. Recently, the use of fluid interfaces has emerged as a way to control the assembly of these systems [11,12]. In the Langmuir-Blodgett technique, for example, a monolayer of 2D nanomaterials is adsorbed at a flat fluid-fluid interface, and the monolayer compressed by barriers [13]. The monolayer is then transferred to a solid substrate [14,15]. Critical to the performance of the resulting particle coating is predicting the particle coverage in the fluid interface upon uniaxial compression in the trough, and whether the particle monolayer displays a solidlike behavior. If the particles jam at the fluid interface, the particle monolayer can buckle, and the signature of this buckling is visible in the profile of surface pressure vs barrier displacement [2,7,16,17]. The analysis of the relation between buckling wavelength and associated force on the barrier discussed in the current paper is therefore relevant for interpreting interfacial rheology measurements with 2D nanomaterials. More broadly, the current investigation could help understanding of the mechanics of particle rafts, armored bubbles, or droplets, a research field that has received increasing attention recently from the soft matter physics, colloidal science, and fluid mechanics communities [18].

II. EXPERIMENTAL METHODS

Uniaxial compression experiments are carried out in an in-house-made rectangular trough of length 200 mm and width $W_t = 50$ mm; see Fig. 1. A stationary barrier mounted on a force sensor allows us to measure the force F on the barrier and the surface pressure $\Pi = F/W_t$. A moving barrier mounted on a linear stage allows us to control the distance Δ between the barriers in steps of 10 μm. To measure forces of the order of mN we use a load cell with a resolution of ± 0.1 mN. For small forces of the order of μN, produced by the smallest particles, we use a cantilever-based force sensor, which is described later in detail.

For the 2D monolayer experiments, we use transparent hexagonal plates made of Mylar (density $\rho_p \simeq 1400\ \mathrm{kg/m^3}$) purchased from Geotech International. The plates have thickness $t = 50$ μm and two different lateral sizes, $L = 1.5$ mm and 3 mm. Here L refers to the inscribed circle diameter of the hexagonal plates. To remove possible contaminants, we aspirate the fluid interface using a suction pipette after moving the barriers to minimum opening [19]. The process is repeated until the fluid interface is clean. The interface is assumed to be clean if the surface pressure at maximum compression is below 4 mN/m. The 2D monolayer is prepared by gently sprinkling the particles on the air-water interface at maximum $\Delta \simeq 3W_t$. Overlapping particles are separated by a stirring rod. The 2D monolayer is then compressed at a velocity of 200 μm/s. The monolayer undergoes out-of-plane deformations, whose amplitude A is measured by the inclined laser line method [20,21]. The technique involves projecting a laser sheet at an angle θ with respect to the particle-laden fluid interface (Fig. 1). The intersection of the laser sheet with the monolayer results in a line that is imaged from the top by a camera. The intersecting line is straight for a flat monolayer and distorted for a deformed monolayer. The out-of-plane deformation amplitude can be calculated from the lateral distortion of the laser line, accounting for a proportionality constant $\tan(\theta)$. In our experiments $\theta \approx 28^\circ$ (see Fig. 1). This angle is measured precisely by measuring $\tan(\theta)$, the factor of conversion between in-plane displacement of the laser line and out-of-plane deformation, for a rectangular block of known height (15 mm) placed on the fluid interface using a microstage [20]. The resolution of the out-of-plane deformation is 60 μm. The novelty of our method is that we use a laser line that sweeps the monolayer. This approach provides a continuous topographic map, instead of the height profile along a single line. To perform the sweep, the laser source is mounted on a linear stage controlled by a stepper motor.

For the single chain experiments, we use square-shaped Mylar plates of lateral sizes $L = 1, 3, 5, 7, 10, 15$, and 20 mm and thickness $t = 125$ μm, except for the 1 mm Mylar plates for which the thickness is $t = 23$ μm. For all the particles the aspect ratio L/t is larger than 23. The smallest plates are manufactured by laser cutting (Optec Laser Systems). Using the length and thickness of the plates and Young's modulus $\simeq 3$ GPa of Mylar, we estimate an Euler buckling threshold for the plates of $\geqslant 240$ mN. Therefore, the plates do not buckle under compression forces of the order of a few mN and are considered to be rigid in our experiments. Experiments are carried out with both a glycerol-air interface and a water-sunflower oil interface; corresponding density differences between the two fluids are $\tilde{\rho} = 1200 \pm 1\ \mathrm{kg/m^3}$ and $80 \pm 1\ \mathrm{kg/m^3}$, respectively, as measured by an Anton Paar density meter (DMA 5000). The surface tensions of the glycerol-air and water-sunflower interfaces are 65 ± 1 mN/m and 26 ± 1 mN/m, respectively, as measured by the pendant drop method in a Dataphysics Goniometer (OCA 25).

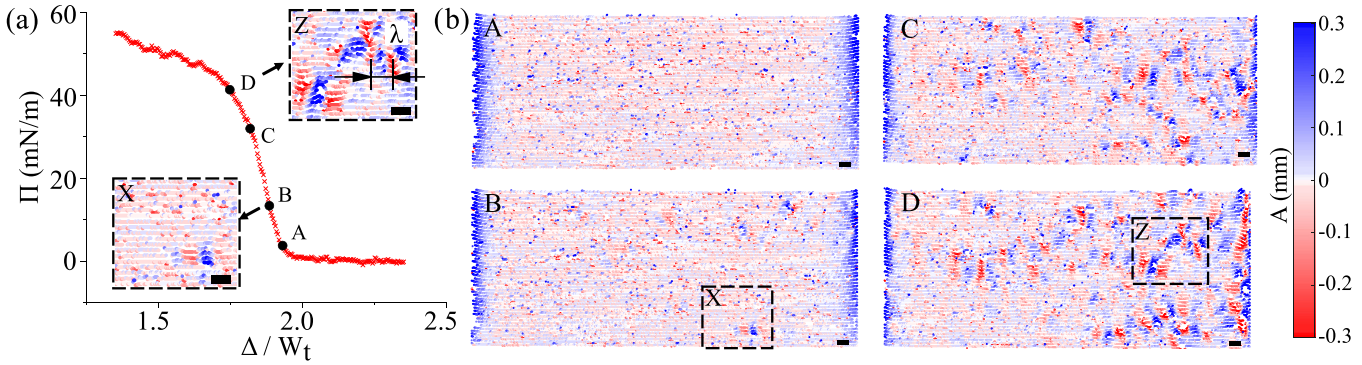

FIG. 2. (a) Surface pressure Π vs normalized separation distance Δ/W_t between the barriers for uniaxial compression of $N \simeq 1590$ hexagonal plates of lateral size 1.5 mm trapped at a water-air interface. We identified four characteristic points A, B, C, and D in correspondence to which the topology of the particle-laden interface is measured. The insets show zoomed-in micro-structures highlighting key features of topology in points B and D. The same data normalized by Δ_0 are shown in Appendix D, where Δ_0 is the compression distance at which the surface pressure becomes finite. (b) Surface topology map of the entire trough area corresponding to the characteristic points in subfigure (a). The blue regions at the left and right ends of the topology maps corresponds to the curved menisci near the barriers. The scale bar shown as a black line is 3 mm, i.e., two particle diameters.

For the water-oil interface, the particles are first arranged at an air-water interface and the oil is gently added. Care is taken to arrange the particles in a straight chain between the barriers. Upon compression, the chain undergoes out of the plane deformation. A camera captures the side view of the chain and from the images we extracted the average amplitude $\langle A \rangle$ of individual plates in the chain. As mentioned earlier, for forces of the order of mN the load cell is used. For forces of the order of few μN we used a cantilever force sensor similar to the micropipette force sensor described in Ref. [22]. The deflection ξ of the cantilever is measured from the side view by a calibrated camera with a zoom lens. The force is computed from $F = k\,\xi$. The stiffness k of the cantilever was obtained by calibration; see Appendix A for the calibration procedure and calibration curves. We used cantilevers of stiffnesses $k = 29$ and 58 μN/mm. The resolution of the force F is ∼1 μN. This value is set by the resolution of the camera ($\simeq$ 11 μm/pixel) and the stiffness of the cantilever.

III. RESULTS

A. Observations on the 2D monolayers

Figure 2(a) shows a typical evolution of the surface pressure $\Pi = F/W_t$ for decreasing values of the normalized distance Δ/W_t between the barriers. Figure 2(b) shows amplitude maps corresponding to four characteristic points of the Π vs Δ curve, denoted A, B, C, and D. For $\Delta/W_t > 2$ the plates are not touching each other and $\Pi \simeq 0$ as expected. As Δ/W_t decreases, contacts between the particles are established and a finite value of Π is measured. In correspondence to point A, $\Pi > 0$ because of the formation of force chains, but the interface remains flat [see panel A in Fig. 2(b)]. Buckling of the monolayer becomes measurable in correspondence to point B. Buckling is evident from the change in amplitude of the particle-laden interface [inset X of Fig. 2(a) and inset X in panel B of Fig. 2(b)]. Further compression leads to an increase in the number of buckled regions as the surface pressure rises. The characteristic point C belongs to this region of behavior. Buckling is predominantly present near the moving barrier [on the right in panel C of Fig. 2(b)]. The point D which we define as the "collapse point" is the value of Δ for which the experimental images start showing the local formation of multilayers. From A to D, the surface pressure increases relatively steeply, while for values Δ/W_t smaller than the one corresponding to D the surface pressure increases comparatively mildly. A video corresponding to the data of Fig. 2 is given in the Supplemental Material [23].

Figure 3(a) shows the tracked laser lines overlaid on a top view of the 2D monolayer. The compression displacement for this figure corresponds to the "collapse point." To measure the local periodicity of the buckled zones (see inset Z of panel D in Fig. 2), we calculated the height-height correlation function $\langle h(x)h(x+\tilde{x})\rangle$ of the out-of-plane deformations along the compression axis x [blue curves in Fig. 3(b)]. The height-height correlation averaged over all the laser lines [black curve in Fig. 3(b)] shows a maximum at $\tilde{x} \approx 3.1L$, which provides evidence that $\lambda \sim L$ for the 1.5 mm plates. For the larger ($L = 3$ mm) plates we measured $\lambda = 2.25L$ for small compression displacement, again suggesting $\lambda \sim L$. The key observation from the height-height correlation function is that the local wavelength in the regions where buckling occurs is of the order of the particle diameter.

For small compression [panel B in Fig. 2(b)] the deformations are localized in a few buckled regions of approximate extent ≈2.4 L in the compression direction. For large compression [panel D in Fig. 2(b)] the height-height correlation indicates a characteristic correlation length of about 3.1 L. Thus the periodicity of the buckled zones is approximately independent of Δ. Also, the monolayer does not show long-range ordered wavelike patterns, as reported for spheres [2]. The fact that no wavelengths much larger than the particle size occur is compatible with a simple model of chain compression, which we now describe.

B. 1D chain model and comparison with experiment

We now analyze the compression of a linear chain of $N = 16$ square plates of size $L = 10$ mm trapped at an air-glycerol interface. The measured force F and the normalized

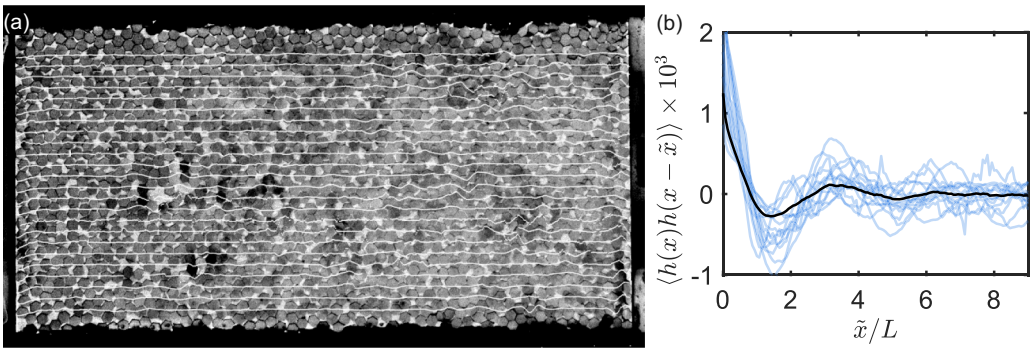

FIG. 3. (a) Tracked laser lines overlaid on the image of plate particle monolayer corresponding to point D of Fig. 2(a). The vertical spacing between the lines is approximately one particle diameter. (b) Height-height correlation functions based on the amplitudes from the tracked laser lines (in blue). The black line is the average over all tracked lines. Here the coordinates x and $\tilde{x}$ are along the compression direction.

average amplitude $\langle A\rangle/L$ of the out-of-plane deformation are shown in Fig. 4 as a function of $\Delta/(NL)$. From this plot, two regimes can be identified. For $\Delta/(NL) > 1$, the distance between the barriers is larger than the total length of the chain. Therefore, $F = 0$ and $\langle A\rangle \simeq 0$ ("flat state"). For $\Delta/(NL) = 1$, the plates touch each other and F starts to increase. The measured average amplitude increases when $\Delta/(NL)$ is approximately equal to 0.9995. The fact that F can be nonzero while $\langle A\rangle \simeq 0$, a feature that was also observed in the 2D system, is due to small particle rearrangements before jamming. The "buckled state" for $\Delta/(NL) < 0.9995$ is characterized by a sharp increase in F followed by a plateau. In the rest of this paper, we will call the plateau value of F the buckling force, as it represents the magnitude of the force that would be required to buckle the monolayer in an experiment conducted at applied force.

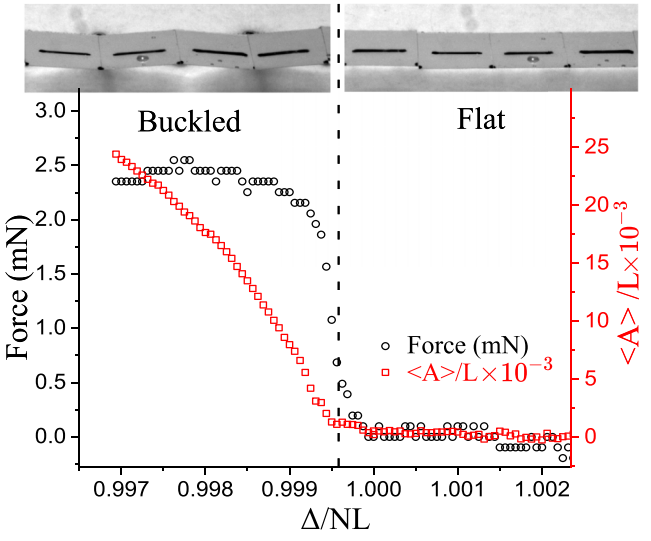

FIG. 4. Single chain compression experiment. Force F (black markers) on the barrier and normalized average amplitude of out-of-plane deformation $\langle A\rangle/L$ (red markers) plotted against normalized distance $\Delta/(NL)$ between the barriers for $N = 16$ square plates of size $L = 10$ mm at a glycerol-air interface. The vertical dashed line at $\Delta/(NL) = 0.9995$ marks the transition from the flat to the buckled state. The two insets illustrate a configuration in the flat state $\Delta/(NL) > 0.9995$ and in the buckled state $\Delta/(NL) < 0.9995$.

The dependence of amplitude on the compression displacement in the buckled state is compared against a simple analytical prediction based on the assumption that the triangular wave is perfectly periodic (see Appendix B). The model predicts the trend correctly, but overestimates the experimental data. Possible explanations for this discrepancy are that the experimental wave is not perfectly periodic and the observed amplitude at the barriers is slightly smaller than the amplitude away from the barrier. The wavelength λ of the monolayer corrugation was obtained by visual inspection. Experiments with different numbers of plates, from 5 to 16, consistently gave $\lambda \simeq 2L$, as shown in the inset of Fig. 4 for $N = 16$.

To analyze the observed behavior, we developed a mathematical model based on a balance between capillary forces, gravity, and contact forces. The total free energy of the system is given by the gravitation potential energy of the fluid (located both below the fluid interface and below the plates) and the interfacial energy of the fluid-fluid interface. Calling $h(x, z)$ the height of the fluid-fluid interface (see Fig. 5), and assuming that the plates pin the contact line at their edges [24], the gravitational potential energy contribution to the total free energy is

$$E_g = \int_0^{\Delta} dx \left[\frac{1}{2}\tilde{\rho} g L h^2(x,0) + 2\int_0^{\infty} \frac{1}{2}\tilde{\rho} g h^2\, dz \right], \quad (1)$$

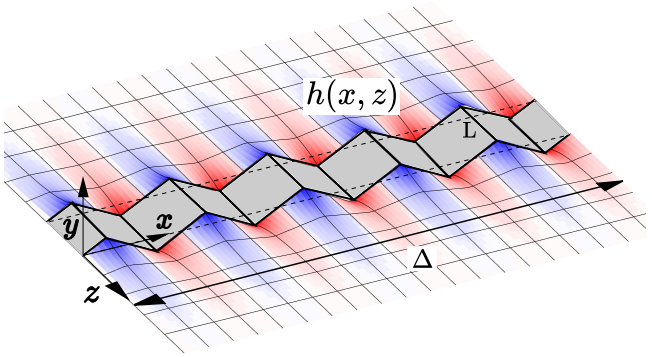

FIG. 5. Sketch of a chain of N plates of length L displaced by $NL - \Delta$. The air-liquid or the liquid-liquid side menisci pinned to the edges of the particles is indicated by $h(x, z)$. The color code indicates the vertical (along the y axis) deformation of the interface.

where $\tilde{\rho} = \rho_l - \rho_a$ is the difference in density between the heavier fluid and the lighter fluid, x is the coordinate along the chain and z is the coordinate perpendicular to the chain in the plane of the unperturbed fluid interface, with $z = 0$ corresponding to the contact line on one side of each plate (see Fig. 5). The first term in Eq. (1) is the gravitational energy of the liquid below the plates, and the second term is the gravitational energy of the liquid in the two side menisci. The capillary energy associated with the menisci on both sides of the chain is

$$E_\gamma = 2\gamma \int_0^\Delta dx \int_0^\infty \sqrt{1 + \left(\frac{\partial h}{\partial x}\right)^2 + \left(\frac{\partial h}{\partial z}\right)^2}\, dz. \tag{2}$$

We neglect the contribution to the capillary energy due to the average displacement of the contact line in the vertical direction caused by the particle weight minus buoyancy, giving rise to the capillary monopole term important in the "Cheerios effect" [25]. The perimeter-averaged vertical interface displacement caused by the plate weight is of the order of $\mathrm{Bo}_p \ell_c$ where $\mathrm{Bo}_p = \rho_p g L t/\gamma$ is the particle Bond number and $\ell_c = \sqrt{\gamma/(\tilde{\rho} g)}$ is the capillary length [26,27]. Based on this estimate, the average vertical contact line displacement is about $0.1\ell_c$. This deformation is not negligible. However, the interfacial energy associated with this displacement is approximately independent of Δ (the particle centers do not translate vertically). Thus the capillary energy contribution due to particle weight towards buckling force or the selection of the dominant buckling mode is negligible. Note that we also neglected the capillary contribution due to the fluid interface in the gap between the particles (i.e., in $-L < z < 0$). To enforce the constraint that the total length of the chain is constant, we add to the total free energy a constraint term

$$E_c = F\left[NL - \int_0^\Delta dx \sqrt{1 + \left(\frac{\partial h}{\partial x}\right)^2\Big|_{z=0}}\right], \tag{3}$$

where F is a scalar Lagrange multiplier. Physically, F represents the contact force between the plates.

The Lagrangian to be minimized is obtained by adding the capillary and gravitational energy contributions, Eqs. (1) and (2), to the Lagrange multiplier term Eq. (3). Imposing $\delta(E_g + E_\gamma + E_c) = 0$, where δ denotes the functional derivative, yields two equations (the full expressions for δE_g, δE_γ and δE_c are given in Appendix C). The first equation is the small-amplitude Young-Laplace equation governing the shape of the fluid-fluid interface for $-L > z > 0$:

$$\tilde{\rho} g h = \gamma\left(\frac{\partial^2 h}{\partial x^2} + \frac{\partial^2 h}{\partial z^2}\right). \tag{4}$$

The second equation is the boundary condition at $z = 0$:

$$\tilde{\rho} g L h - 2\gamma \frac{\partial h}{\partial z} + F\frac{\partial^2 h}{\partial x^2} = 0. \tag{5}$$

The small amplitude assumption holds for the 1D chain because the maximum amplitude is only $A/L \simeq 2.5 \times 10^{-2}$ (see Fig. 4). Upon multiplication by L, Eq. (5) is a balance of moments. The first term represents the moment of the hydrostatic pressure force due to the weight of the fluid below the plates. The second term represents the moment of the vertical projection of the surface tension force at the contact line, located at $z = 0$ and $z = -L$. The third term represents the moment of the contact forces F between the particles.

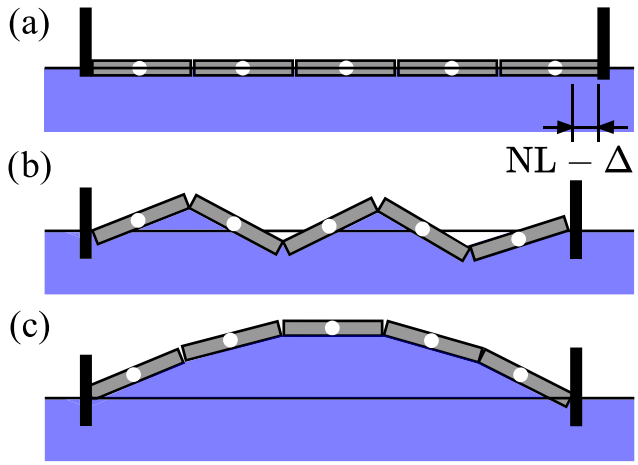

FIG. 6. Upon compression of an initially flat monolayer (a), both configuration (b) and configuration (c) are solutions to Eq. (5). We observe only configuration (b).

The leading-order Fourier mode solution of Eq. (4) that matches the triangle-wave profile of the contact line is [28]

$$h(x, z) = A e^{-z\sqrt{\left(\frac{2\pi}{\lambda}\right)^2 + \frac{1}{\ell_c^2}}} \sin\left(\frac{2\pi x}{\lambda}\right), \tag{6}$$

where $\ell_c = \sqrt{\gamma/\tilde{\rho} g}$ is the capillary length. Equation (6) satisfies $h(x, z = 0) = A\sin(2\pi x/\lambda)$ and $h(x, z \to \infty) = 0$. For $\lambda \gg \ell_c$ and $\lambda \ll \ell_c$, the decay lengths of the meniscus in the z direction are ℓ_c and $\lambda/2\pi$, respectively. Thus, in the surface tension-dominated regime the buckling wavelength and the decay length of the fluid interface distortion are roughly of the same order of magnitude.

Substituting Eq. (6) into Eq. (5) yields the contact force as a function of the wavelength:

$$F = \frac{1}{4\pi^2}\tilde{\rho} g L \lambda^2 + \frac{1}{2\pi^2}\gamma\lambda\sqrt{(2\pi)^2 + \left(\frac{\lambda}{\ell_c}\right)^2}. \tag{7}$$

Because of the small-amplitude assumption the buckling force is independent of A. The capillary energy, the gravitational energies and the constraint term are proportional to NL in the limit of small compression displacement (since $\Delta \approx NL$). Therefore, the buckling force is also independent of N. In Fig. 6 we show two configurations of buckled chains, with $\lambda = 2L$ in configuration (b) and $\lambda = 10L$ in configuration (c). While both wavelengths are solutions to Eq. (5), the absolute minimum of $F(\lambda)$ is the total energy minimum, as in the buckling of an Euler beam [29]. Since $F(\lambda)$ is a monotonically increasing function of λ and wavelengths smaller than $2L$ are not possible, the equilibrium wavelength is

$$\lambda = 2L. \tag{8}$$

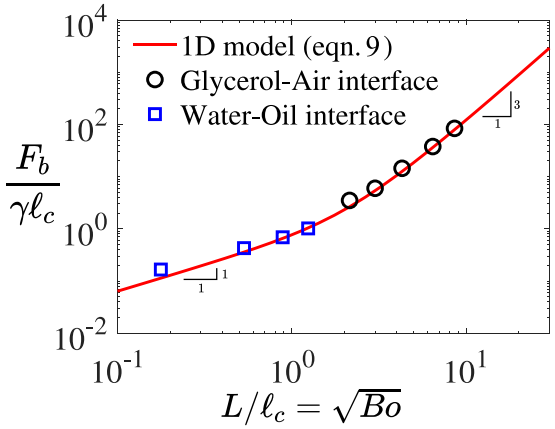

FIG. 7. Normalized buckling force $F_b/(\gamma \ell_c)$ vs normalized particle length L/ℓ_c for the 1D chain experiments. The markers correspond to experimental data, blue squares for chains at a water-oil interface, and black circles for chains at a glycerol-air interface. The red line is Eq. (9).

The contact force corresponding to $\lambda = 2L$ is the buckling force:

$$\frac{F_b}{\gamma \ell_c} = \frac{1}{\pi^2}\left(\frac{L}{\ell_c}\right)^3 + \frac{2}{\pi}\frac{L}{\ell_c}\sqrt{1+\left(\frac{L}{\pi \ell_c}\right)^2}. \tag{9}$$

Figure 7 shows $F_b/(\gamma \ell_c)$ vs $\sqrt{\mathrm{Bo}} = L/\ell_c$, comparing Eq. (9) with the experimental data. Here $\mathrm{Bo} = \tilde{\rho} g L^2/\gamma$. Despite Eq. (9) having no free parameters, the agreement between the experimental data and the theory is excellent, except for the smallest values of Bo for which a perfect alignment of the plates cannot be ensured. For $\mathrm{Bo} \gg 1$ the gravitational force dominates and $F_b \sim \tilde{\rho} g L^3$. In this regime, the buckling force is of the order of the weight of the liquid displaced by each plate as the chain deforms. For $\mathrm{Bo} \ll 1$, $F_b \sim \gamma L$. In this regime, the buckling force is of the order of the capillary force exerted by the side meniscus on each plate. Equating the first and second terms in Eq. (9) provides a threshold $L/\ell_c \simeq \pi$ for the transition between the capillarity- and gravity-dominated regimes.

Reference [30] reports compression experiments performed on an air bubble covered with a monolayer of spherical particles. The data show both smooth buckling indentations of the order of the bubble size and small-scale undulations of the order of the particle size. The authors explain the appearance of the small-scale undulations with a discrete model that includes a capillary energy contribution due to displacement of each particle from the plane of the fluid interface. Similar to ours, this model does not treat the particle monolayer as an elastic membrane (the model, however, does not include capillary-induced bending energy contributions, which could be important for spheres [1,31]). The scaling predicted by this model is similar to ours, but the physics is different: in our case the particle centers of mass do not translate with respect to the average plane of the interface when the dominant, small wavelength mode is selected [see Fig. 6(b)]. However, the experiments are interesting because they show that small-scale undulations could be superimposed on smoother ones in the case of spherical particles embedded in curved fluid interfaces.

C. Comparison of 1D model with 2D experiment

It is instructive to compare the prediction of the chain model to the experimental data for the 2D monolayer. The model predicts $\lambda = 2L$, close to the peak-to-peak value in the height-height correlation function measured from the 2D monolayer data (see Sec. III A). A peak-to-peak distance slightly larger than $\lambda = 2L$ is expected because the buckled regions are not exactly perpendicular to the laser line (for a nonzero angle between the laser line and the buckling direction, the measured peak-to-peak distance in the correlation function is larger than the actual separation between the "crests" of the monolayer).

A comparison between an estimate of the surface pressure obtained from 1D model and the measured surface pressure for 2D system [see Fig. 2(a)] is also possible. The buckling surface pressure from Eq. (9) is

$$\Pi_b = \frac{F_b}{L} = \frac{1}{\pi^2}\tilde{\rho} g L^2 + \frac{1}{\pi^2}\gamma\sqrt{(2\pi)^2 + \left(\frac{2L}{\ell_c}\right)^2}. \tag{10}$$

Such a comparison should account for two differences. First, in the 1D chain the internal stress in the monolayer due to particle-particle contact forces is essentially homogeneous along the compression direction (on a scale $\gg L$). In the 2D assembly, the contact forces are instead a random function of position and orientation. Second, in the 2D monolayer the balance of forces on the entire monolayer should account for friction with the lateral walls [32,33]. Evidence of the importance of the lateral walls in our experiments is the fact that the amplitude of the monolayer deformation is larger near the moving barrier [see panels C and D in Fig. 2(b)]. A larger deformation occurs in this region because the gradient of the surface pressure along the compression direction must balance the frictional stresses on the lateral walls, leading to a larger surface pressure and deformations near the moving barrier. However, the 1D chain model could still provide an estimate of the average value of Π in regions where buckling occurs and sufficiently away from the lateral walls.

We performed buckling experiments at different trough aspect ratios. Trough aspect ratios are changed by varying the number of particles between the barriers for a fixed trough width. The particle size is fixed to $L = 1.5$ mm in all experiments. Figure 8 shows the surface pressure profiles for the 2D monolayer as a function of Δ/W_t for $N \simeq 330$–2040. We see from this curve that the surface pressure profile depends on the initial trough area, another manifestation of the effect of lateral wall friction [32–34].

Figure 9 shows the experimental data for the surface pressure in the 2D monolayer, averaged over three different measurements, for different values of Δ/W_t. This figure is obtained from Fig. 8 by reporting the value of Π and Δ/W_t corresponding to the collapse point D. In order to compare the collapse surface pressure in the 2D monolayer with the 1D model we used a Coulomb model for the lateral wall friction as done in [32] for a monolayer of spherical particles. This model assumes that the frictional force per unit length is proportional to the local values of Π according to a proportionality constant μ_{wall}. This approximation yields an exponential decay law also referred to as the Janssen model, $\Pi = \Pi_0 \exp(-2\mu_{\mathrm{wall}}\nu\Delta/W_t)$ [32]. Here Π_0 is the pressure

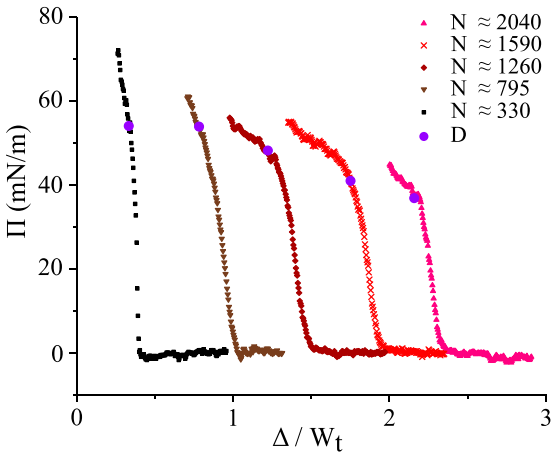

FIG. 8. Surface pressure Π measured at the stationary barrier for 2D monolayers of $L = 1.5$ mm hexagonal particles at a water-air interface against the distance between the barriers normalized by the trough width Δ/W_t for different number of plates. The points D (in purple markers) are the collapse points.

at the moving barrier and ν is the ratio of surface pressures perpendicular and parallel to the compression direction. Assuming $\nu = 1/3$ [32], the best fit to the data (dashed curve in Fig. 9) gives $\Pi_0 = 53.8$ mN/m and $\mu_{\text{wall}} = 0.24$. The trough walls are made of PLA plastic. While we could not find the data for the friction coefficient of Mylar on PLA in water, the reported friction coefficients for Mylar against different engineering materials such as copper and wood are in the range 0.13–0.41 [35]. The black square dot in Fig. 9 is the extrapolation of the experimental data for the 2D monolayer to $\Delta/W_t = 0$, which yields $\Pi_0 = 53.8$ mN/m. The red square dot in Fig. 9 is obtained by using the parameters of our problem in Eq. (10). The value of Π_0 from the friction model

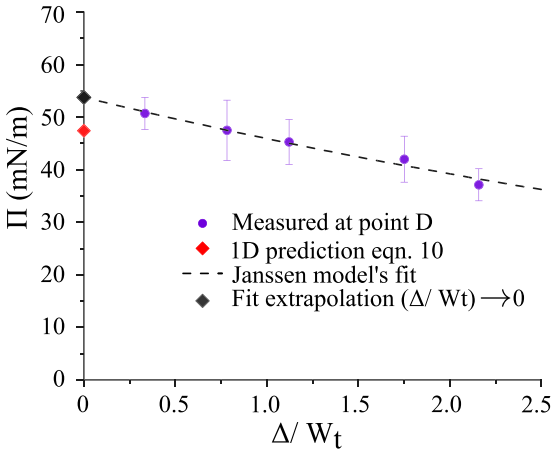

FIG. 9. Surface pressure at collapse point D for 2D monolayers of $L = 1.5$ mm hexagonal particles at a water-air interface, averaged over three realizations and plotted against the distance between the barriers (normalized by the trough width). The error bars represent the standard deviations. The dashed curve is the Janssen model's fit to the experimental data. The black marker is the extrapolation of the Janssen model's fit for $\Delta/W_t \to 0$. The red marker is the surface pressure predicted by the 1D chain model (10).

is larger than the value from the 1D chain model, but the difference is small (about 13%). Considering the simplicity of the chain model, the agreement with the 2D data is surprisingly good. We would like to emphasize that, given the limited range of Δ, we cannot establish the full validity of Janssen model for our system. The fitting via this model is used here only to illustrate the effect of lateral wall friction on the expected trend of Π and the limited effect of friction in the limit $\Delta/W_t \to 0$.

As stated before, the 2D monolayer differs from the 1D chain in the distribution of contact forces between the particles. Statistics of contact forces between jammed particles have been studied extensively in the context of granular materials [34,36–38]. These studies reveal that the probability of contact forces attaining a value f larger than the mean value $\langle f \rangle$ decays fast, approximately as $p(f/\langle f \rangle) \sim \exp(-\beta f/\langle f \rangle)$ with β an $O(1)$ numerical coefficient [34,36–38]. Therefore it is expected that the monolayer contains few contact forces that are large compared to the average contact force [34]. Upon monolayer compression, the first buckling events will occur for groups of particles for which the contact force exceeds the estimate in Eq. (9). Because such large forces are small in number, the buckling regions are initially localized, as seen in panel B in Fig. 2(b). If the mechanical response of the monolayer is dominated by these spatially scattered regions, Eq. (10) could provide an upper bound for the surface pressure measured at the barrier in the 2D experiment.

In our experiments the buckled zones do not show long-range periodicity. Even for large compression displacements the average height-height correlation function becomes negligible for $\tilde{x} \approx 7L$ [see Fig. 3(b)]. A possible explanation is spatial localization of forces chains. Studies on jammed granular packing reveal that the force chains do not extend over more than a few particle diameters [39,40].

In the 1D chain, the decay length of the side meniscus is $L/\pi \sim 0.3L$ in the capillary regime. In a randomly packed 2D system, the average distance between the edges of the particle is $L(1/\sqrt{\phi} - 1)$, where ϕ is the surface fraction of the plate particles. For $\phi \simeq 0.84$, the value appropriate for a random close packing of disks [33], we obtain an average distance of $\simeq 0.1L$ between the particle edges. Therefore, in the capillary regime the meniscus decay length and the distance between the particle edges are of the same order of magnitude. Because of this, the solution for the 1D chain could be used as a local approximation to the contact force in the 2D system. In the gravity-dominated regime the side meniscus deformation gives a negligible contribution to the contact force, so also in this regime the application of the 1D model to the 2D system is justified as a first approximation.

D. 1D model with bending rigidity

Key in our derivations is the absence of bending energy in the energy functional. Experiments with graphene oxide [5] seem to be compatible with the our model, but the observed wavelength is slightly larger than $2L$. A possible explanation for observing wavelengths larger than $2L$ could be the presence of a small but finite bending rigidity of the monolayer. An extension of Eq. (5) accounting for an effective monolayer

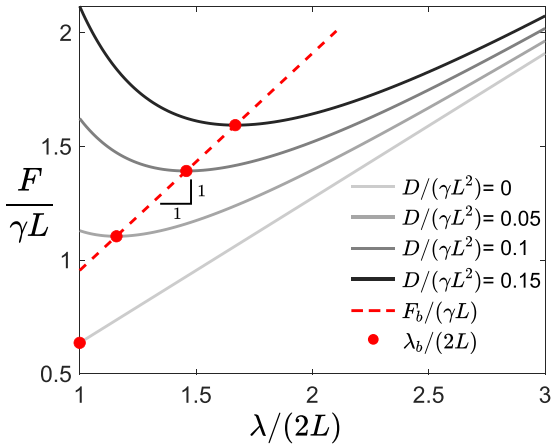

FIG. 10. Normalized force $F/(\gamma L)$ as a function of normalized wavelength $\lambda/(2L)$ for small values of normalized bending rigidity and Bo = 0 [see Eq. (14)].

bending rigidity (per unit width) D is

$$DL\frac{\partial^4 h}{\partial x^4} + \tilde{\rho} g h L - 2\gamma \frac{\partial h}{\partial z} + F\frac{\partial^2 h}{\partial x^2} = 0, \tag{11}$$

and substituting Eq. (6) into Eq. (11) gives

$$\frac{F}{\gamma L} = \frac{D}{\gamma L^2}\left(\frac{2\pi L}{\lambda}\right)^2 + 2\left(\frac{\lambda}{2\pi L}\right)\sqrt{1 + \mathrm{Bo}\left(\frac{\lambda}{2\pi L}\right)^2} + \mathrm{Bo}\left(\frac{\lambda}{2\pi L}\right)^2. \tag{12}$$

For $\gamma = 0$ Eqs. (11) and (12) predicts $\lambda_b = (D/\tilde{\rho} g)^{1/4}$, which is the result of Ref. [4]. For $D/(\gamma L^2) \ll 1$ bending rigidity effects are negligible, and we recover the results of Sec. III b. For intermediate values of $D/(\gamma L^2)$, the wavelength that minimizes the force is larger than $2L$. Its precise value can be found by solving $dF/d\lambda = 0$. For Bo $\ll 1$, gravity becomes negligible and the buckling mechanics is dominated by bending rigidity and capillary forces. The buckling wavelength in this limit is

$$\frac{\lambda_b}{2L} = \max\left\{1,\ \pi\left(\frac{D}{\gamma L^2}\right)^{1/3}\right\}, \tag{13}$$

and the corresponding buckling force is

$$\frac{F_b}{\gamma L} = \max\left\{\frac{2}{\pi},\ 3\left(\frac{D}{\gamma L^2}\right)^{1/3}\right\}. \tag{14}$$

Figure 10 shows $F/(\gamma L)$ vs $\lambda/(2L)$ for Bo = 0 and selected small values of $D/(\gamma L^2)$. The wavelength that minimizes F is indicated by the red dots. From Eqs. (13) and (14) we see that both the buckling wavelength and buckling force are proportional to $[D/(\gamma L^2)]^{1/3}$, thus $F_b \propto \lambda_b$ (red dashed line in Fig. 10). For increasing values of $D/(\gamma L^2)$ the wavelength that minimizes the force becomes larger than $2L$.

In an interfacial monolayer of 2D nanosheets, the nanosheets can overlap slightly [13,41,42]. This overlap can result in a small but finite effective bending rigidity because of the attractive force between the sheets in the overlapping region. In Ref. [43] a Lennard-Jones potential was used to model the attractive interaction potential between parallel sheets of graphene. Using the Lennard-Jones potential, and assuming that the angle between pairs of overlapping sheets is small, it is easy to estimate the effective bending rigidity corresponding to an average overlap length ℓ (see Appendix E):

$$D \simeq \frac{40\Gamma L \ell^3}{3r_0^2}. \tag{15}$$

Here Γ is the adhesion energy per unit area and r_0 is the nanometric equilibrium separation between the nearly-parallel sheets. The model suggests a strong ℓ^3 scaling with the overlap length. For graphene oxide sheets in high-humidity conditions, molecular dynamics simulations suggest $r_0 \simeq$ 7.7–12 Å [44,45] and $\Gamma \simeq 0.1$–0.2 J/m^2 [42,46]. Taking realistic values $\Gamma = 0.2$ J/m^2, and $r_0 = 12$ Å and an average sheet length $L = 1$ μm, $D/(\gamma L^2)$ is estimated to be 0.02 and 26 for $\ell = 1$ nm and 10 nm, respectively (assuming the surface tension of water, $\gamma = 0.07$ J/m^2). The corresponding wavelengths are 2 μm and 20 μm, respectively. An overlap length of 1 nm does not change the wavelength appreciably from $2L$, whereas an overlap length of 10 nm increases the buckling wavelength to $20L$. For a randomly distributed overlap lengths between 1 and 10 nm, the predicted wavelength range is 2–$20L$, which is is similar to wavelength range observed in the experiments with graphene oxide [5]. The inclusion of the effect of overlaps therefore enables the analytical prediction developed for small amplitudes to be closer to the experimental data for graphene oxide nanoparticles.

IV. CONCLUSIONS

We measured the amplitude of deformation, wavelength, and force on the barrier for a 2D and 1D monolayer of plates trapped at a fluid-fluid interface and subject to uniaxial compression. The amplitude and wavelength of the corrugations of the 2D monolayer were measured by a laser scanning technique.

The model we developed to predict the experimental data for the linear chain (1D monolayer) predicts the buckling force well over a wide range of values of L/ℓ_c, where ℓ_c is the capillary length and L is the particle length, and without adjustable parameters (Fig. 7). The 1D chain model provides a reasonable order of magnitude estimate of the buckling surface pressure Π for the 2D monolayer, provided that this pressure is identified as the collapse pressure corresponding to the point D in Figs. 2 and 8. The chain model does not contain a dependence on the trough aspect ratio Δ/W_t, but the inclusion of frictional forces with the lateral wall via a Coulomb friction model enables us to model the observed dependence of Π on Δ/W_t. A more complete model should include statistics of force chains, for which theories developed for 2D granular systems [47,48] could be applicable.

The chain model predicts a buckling wavelength $\lambda = 2L$, independent of L/ℓ_c. The 2D monolayer does not display a regular wave pattern, but the characteristic local wavelength in the regions where buckling occurs is of the order of the particle size, as in the 1D chain model. Uniaxial compression of monolayers of spherical particles gives smooth undulations

with a wavelength $\lambda \sim \sqrt{\ell_c L}$ [1], different from the one we observe. In our case the effective bending rigidity of the monolayer is negligible, as the plates can "hinge" at their contact points without a bending energy penalty. In the case of spheres, even in the absence of colloidal force contribution bending energy can originate from the motion of the contact line on the surface of each particle as the mean interface curvature changes [31]. An indication of this is that the order of magnitude of the effective bending rigidity corresponding to $\lambda \sim \sqrt{\ell_c L}$ is $\gamma\ d^2$; this can be seen as the change in interfacial energy as a sphere of diameter d protrudes in the fluid interface over a distance comparable to d. In our case the undulations of the contact line relative to the particles, if present, are at most limited to a scale $t \ll L$, where t is the particle thickness. The corresponding changes in interfacial energy upon a change in interfacial curvature is $O(\gamma L t)$ [24,49]. For $L/\ell_c \ll 1$ and $t/L \ll 1$, this contribution is negligible in comparison to the dominant contribution, of order $\gamma A\lambda \sim \gamma L^2$, due to the rotation of each particle as the monolayer is compressed. In Ref. [2] a scaling $\lambda \propto L$ was reported for experiments with spheres, but only for very small compressive displacements, whereas $\lambda \propto \sqrt{L}$ was observed for larger displacements. Perhaps this transition could be the result of depinning of the contact line at large compression. These comparisons suggest that both the particle aspect ratio and contact line motion could determine the characteristic buckling wavelength.

In our experiments we prepare the particle-laden interface ensuring no initial overlaps. If a monolayer of 2D nanosheets is prepared with care, overlaps can be largely prevented (nanosheet stacking requires overcoming an energy barrier [41]), but probably not completely eliminated at large degrees of compression. Tuning the pH of the liquid [7] or adding surfactants [16] has been shown to suppress the stacking of 2D materials at fluid interfaces, so one may realize the experimental systems described in the current paper using real 2D materials. If particle overlaps did occur even before the compression of the particle-laden interface, the analysis would need to account for particle-particle interactions as well as statistics of the geometry of the overlapping regions. Overlaps contribute to a nonzero bending rigidity as a result of the adhesion forces between the nanosheets. We have shown mathematically that this effect increases the buckling wavelength compared to $2L$ (see Fig. 10).

Compression of platelike particles trapped at fluid interfaces occurs in a variety of applied settings, for instance, in the manufacturing of thin films [13,16,50], in the deformation of Pickering emulsions [10,51], or in the production of crumpled graphene by aerosolization [52]. This work contributes to our understanding of the link between particle shape, contact mechanics, and response of the fluid interface during the compression of monolayers of platelike particles of controlled geometry.

ACKNOWLEDGMENTS

We thank Simon Gravelle and Adyant Agarwal for useful discussions on modeling the interaction energy between two nanosheets. We thank Paul Grandgeorge for useful suggestions on force measurements in the μN range. We gratefully acknowledge funding by the European Research Council (ERC) under the European Unions Horizon 2020 Research and Innovation program (Project FLEXNANOFLOW, Grant No. 715475).

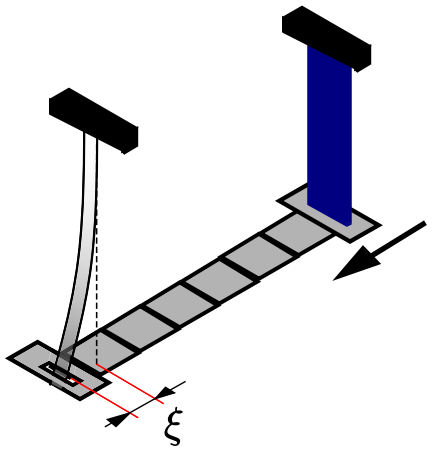

FIG. 11. Forces measurement with cantilever force sensor.

APPENDIX A: MICRO FORCE SENSOR

The cantilever force sensors are Mylar sheets with lengths of 80 and 100 mm, width of 10 mm, and thickness of 125 μm. One end of the sheet is clamped, and the free end is unconstrained. The free end is passed through another Mylar sheet, with a rectangular hole, which acts as the barrier (see Fig. 11). The deflection of the Mylar sheet (ξ) from its undeformed position is calculated by imaging from the side view.

To calibrate the force sensors, the fixed end of the cantilever is mounted on a manual precision stage and the free end sits on a knife edge placed on a Mettler Toledo precision microbalance (see inset of Fig. 12). Imposing successive displacements of 0.5 mm via the manual precision stage, the corresponding forces are read from the balance. Figure 12 shows force vs displacement of the manual stage. The force is linear with respect to the displacement for displacements as

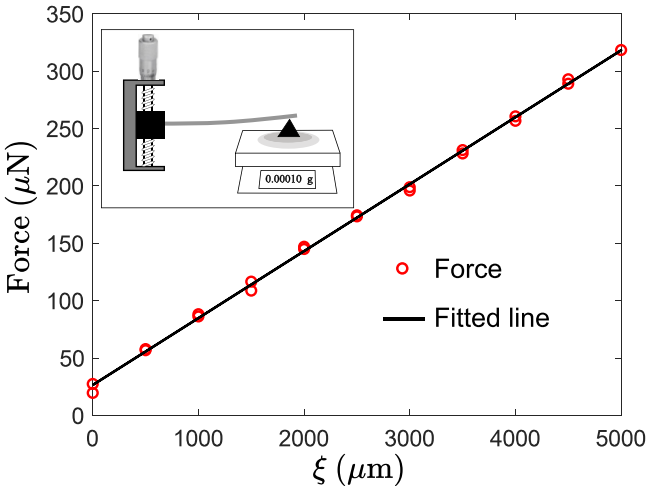

FIG. 12. Calibration curve of the force sensor. The inset shows the schematic of force sensor calibration with precision balance.

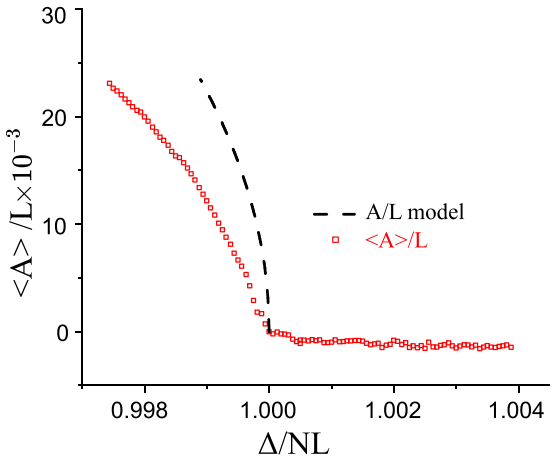

FIG. 13. Amplitude data in Fig. 4 plotted against the analytical prediction $A/L = (1/2)\sqrt{1-[\Delta/(NL)]^2}$.

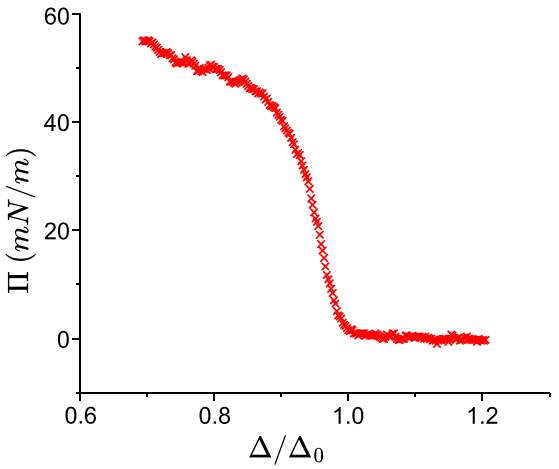

FIG. 14. Surface pressure Π vs normalized separation distance Δ/Δ_0, where Δ_0 is the compression distance at which Π becomes finite.

large as 5 mm. The slope of the line fitted to the experimental data gives the stiffness k of the beam.

APPENDIX B: DEPENDENCE OF AMPLITUDE ON Δ IN 1D EXPERIMENTS

A simple geometric argument assuming that the buckled 1D system is a perfectly periodic triangular wave gives $A/L = (1/2)\sqrt{1-[\Delta/(NL)]^2}$ (without considering boundary effects). In Fig. 13 we compare this analytical prediction to the experimental data for the mean amplitude from the 1D experiments (see Fig. 4). To enable the comparison, we shift the experimental data so that $\langle A\rangle = 0$ exactly when $\Delta = NL$. It can be seen that the simple model gives the correct trend. However, it overpredicts the mean amplitude by about 40%.

APPENDIX C: EULER-LAGRANGE MINIMIZATION

The variation of the gravitational energy in the 1D model is

$$\delta E_g = \int_0^{\Delta} dx \tilde{\rho} g L h_0 \delta h_0 + 2\int_0^{\Delta} dx \int_0^{\infty} \tilde{\rho} g h \delta h \, dz.$$

Here $h_0 = h(x, z = 0)$. The variation of the capillary energy is

$$\delta E_\gamma \simeq 2\gamma \int_0^{\infty} [h_x \delta h]_0^{\Delta} dz + 2\gamma \int_0^{\Delta} [h_z \delta h]_0^{\infty} dx - 2\gamma \int_0^{\infty}\int_0^{\Delta} (h_{xx} + h_{zz})\delta h \, dx \, dz,$$

and the variation in length constraint evaluated at $z = 0$ is

$$\delta E_c = -F[h_{0_x}\delta h_0]_0^{\Delta} + F\int_0^{\Delta} h_{0_{xx}}\delta h_0 \, dx.$$

At equilibrium, the sum $\delta(E_g + E_\gamma + E_c)$ must be zero for an arbitrary δh and $\delta h0$, from which we get Eqs. (4) and (5), respectively.

APPENDIX D: SURFACE PRESSURE VS Δ/Δ_0

Figure 14 shows the data presented in Fig. 2(a) with a different normalization for compression displacement Δ.

APPENDIX E: BENDING RIGIDITY DUE TO OVERLAP BETWEEN TWO ADHESIVE PLATES

The equilibrium distance between two nanosheets is determined by the competition between the attractive van der Waals and the repulsive electrostatic forces between the solid surfaces. A Lennard-Jones potential has been used to model the interaction between two nanosheets in [53,54]. We use the standard 4–10 Lennard-Jones potential energy of interaction (per unit area) between two thin parallel plates [43]:

$$\phi(r) = \frac{\Gamma}{3}[5(r_0/r)^4 - 2(r_0/r)^{10}],$$

where r is the separation distance between the plates, r_0 is the equilibrium separation, and $\Gamma = \phi(\infty) - \phi(r_0)$ is the adhesion energy. If the separation distance $r > r_0$ the plates attract each other due to van der Waals forces, and if $r < r_0$ the plates repel each other due to electrostatic forces. For small displacement around r_0, a quadratic approximation to the energy per unit area is [54]

$$\phi(r) \simeq \frac{20\Gamma}{r_0^2}(r - r_0)^2.$$

We consider a 1D chain of platelike particles at a fluid interface where each particle pair has a small overlap of length ℓ (see Fig. 15). We model the interface as a continuous curve parameterized by $\theta(s)$, the local rotation angle along the curvilinear coordinate s. The configuration of a single overlap is illustrated in the inset of Fig. 15. In this figure we take r in the direction normal to the top plate and ζ in the direction tangential to the top plate. Under compression the plates rotate with respect to each other by an angle $d\theta$. The displacement of the second plate is $r(\zeta) = r_0 + \zeta \tan(d\theta)$ (see Fig. 15). The

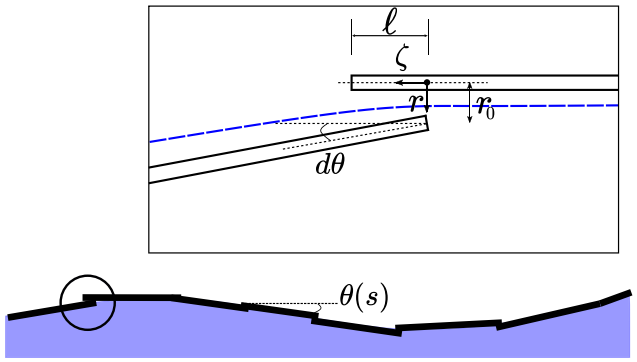

FIG. 15. Schematic of a fluid interface populated by slightly overlapping sheets. The inset shows the zoom of the overlap region. The blue dashed line is the average position of the particle-laden fluid interface.

energy required to impose this rotation for a particle pair is

$$dE \simeq w \int_0^{\ell} \frac{20\Gamma}{r_0^2}(r(\zeta) - r_0)^2 \, d\zeta \, .$$

Carrying out the integration for $|d\theta| \ll 1$ we obtain

$$dE \simeq \frac{w}{2}\left(\frac{40\Gamma\ell^3}{3r_0^2}\right)d\theta^2$$

When we multiply and divide by $(ds)^2$, where ds is an infinitesimal element of curvilinear coordinate, we obtain

$$dE \simeq \frac{w}{2}\left(\frac{40\Gamma\ell^3}{3r_0^2}\, ds\right)\left(\frac{d\theta}{ds}\right)^2 ds. \tag{E1}$$

For a continuous surface, the bending rigidity D (per unit width) is defined so that $dE = \frac{1}{2} w D \kappa^2 \, ds$, where $\kappa = d\theta/ds$ is the curvature. Comparing this expression to Eq. (E1) we obtain $D = (40\Gamma\ell^3)/(3r_0^2)\, ds$. In our case, because dE represents the energy per particle pair, ds is the distance between two particle centers, i.e., $ds = L - \ell$. For $\ell \ll L$ the estimate of the bending rigidity is $D = (40\Gamma\ell^3)/(3r_0^2)L$, as in Eq. (15). The assumption of a continuous surface is reasonable if $N \gg 1$, where N is the total number of plates [55]. The bending rigidity thus scales proportionally to the adhesion energy Γ and depends strongly on the overlap length ℓ.

[1] D. Vella, P. Aussillous, and L. Mahadevan, Elasticity of an interfacial particle raft, Europhys. Lett. **68**, 212 (2004).

[2] E. Jambon-Puillet, C. Josserand, and S. Protière, Wrinkles, folds, and plasticity in granular rafts, Phys. Rev. Mater. **1**, 042601(R) (2017).

[3] B. P. Binks, Particles as surfactants similarities and differences, Curr. Opin. Colloid Interface Sci. **7**, 21 (2002).

[4] L. Pocivavsek, R. Dellsy, A. Kern, S. Johnson, B. Lin, K. Y. C. Lee, and E. Cerda, Stress and fold localization in thin elastic membranes, Science **320**, 912 (2008).

[5] L. Imperiali, K.-H. Liao, C. Clasen, J. Fransaer, C. W. Macosko, and J. Vermant, Interfacial rheology and structure of tiled graphene oxide sheets, Langmuir **28**, 7990 (2012).

[6] S. P. Ogilvie, M. J. Large, M. A. OMara, P. J. Lynch, C. L. Lee, A. A. King, C. Backes, and A. B. Dalton, Size selection of liquid-exfoliated 2D nanosheets, 2D Mater. **6**, 031002 (2019).

[7] L. J. Cote, J. Kim, Z. Zhang, C. Sun, and J. Huang, Tunable assembly of graphene oxide surfactant sheets: Wrinkles, overlaps and impacts on thin film properties, Soft Matter **6**, 6096 (2010).

[8] L. Botto, E. P. Lewandowski, M. Cavallaro, and K. J. Stebe, Capillary interactions between anisotropic particles, Soft Matter **8**, 9957 (2012).

[9] V. Nicolosi, M. Chhowalla, M. G. Kanatzidis, M. S. Strano, and J. N. Coleman, Liquid exfoliation of layered materials, Science **340**, 1226419 (2013).

[10] M. Vis, J. Opdam, I. S. Vant Oor, G. Soligno, R. Van Roij, R. H. Tromp, and B. H. Erné, Water-in-water emulsions stabilized by nanoplates, ACS Macro Lett. **4**, 965 (2015).

[11] A. Fahimi, I. Jurewicz, R. J. Smith, C. S. Sharrock, D. A. Bradley, S. J. Henley, J. N. Coleman, and A. B. Dalton, Density controlled conductivity of pristine graphene films, Carbon **64**, 435 (2013).

[12] S. J. Woltornist, A. J. Oyer, J.-M. Y. Carrillo, A. V. Dobrynin, and D. H. Adamson, Conductive thin films of pristine graphene by solvent interface trapping, ACS Nano **7**, 7062 (2013).

[13] L. J. Cote, F. Kim, and J. Huang, Langmuir-Blodgett assembly of graphite oxide single layers, J. Am. Chem. Soc. **131**, 1043 (2009).

[14] S. Biswas and L. T. Drzal, A novel approach to create a highly ordered monolayer film of graphene nanosheets at the liquid-liquid interface, Nano Lett. **9**, 167 (2009).

[15] J. Neilson, M. P. Avery, and B. Derby, Tiled monolayer films of 2D molybdenum disulfide nanoflakes assembled at liquid/liquid interfaces, ACS Appl. Mater. Interfaces **12**, 25125 (2020).

[16] G. J. Silverberg and C. D. Vecitis, Wrinkling and periodic folding of graphene oxide monolayers by Langmuir–Blodgett compression, Langmuir **33**, 9880 (2017).

[17] G. J. Silverberg, A. A. McClelland, S. Griesse-Nascimento, C. Girabawe, J. P. Kadow, L. Mahadevan, and C. D. Vecitis, Controlling the roughness of Langmuir–Blodgett monolayers, J. Phys. Chem. B **121**, 5078 (2017).

[18] S. Protière, Particle rafts and armored droplets, Annu. Rev. Fluid Mech. **55**, 459 (2023).

[19] S. Razavi, K. D. Cao, B. Lin, K. Y. C. Lee, R. S. Tu, and I. Kretzschmar, Collapse of particle-laden interfaces under compression: Buckling vs particle expulsion, Langmuir **31**, 7764 (2015).

[20] F. Boyer, O. Pouliquen, and É. Guazzelli, Dense suspensions in rotating-rod flows: Normal stresses and particle migration, J. Fluid Mech. **686**, 5 (2011).

[21] H. Perrin, M. Wyart, B. Metzger, and Y. Forterre, Nonlocal effects reflect the jamming criticality in frictionless granular flows down inclines, Phys. Rev. Lett. **126**, 228002 (2021).

[22] M. Backholm and O. Bäumchen, Micropipette force sensors for in vivo force measurements on single cells and multicellular microorganisms, Nat. Protoc. **14**, 594 (2019).

[23] See Supplemental Material at http://link.aps.org/supplemental/10.1103/PhysRevE.109.014801 for the video corresponding to the data of Fig. 2.

[24] L. Yao, N. Sharifi-Mood, I. B. Liu, and K. J. Stebe, Capillary migration of microdisks on curved interfaces, J. Colloid Interface Sci. **449**, 436 (2015).
[25] D. Vella and L. Mahadevan, The "Cheerios effect", Am. J. Phys. **73**, 817 (2005).
[26] T. I. Hesla and D. D. Joseph, The maximum contact angle at the rim of a heavy floating disk, J. Colloid Interface Sci. **279**, 186 (2004).
[27] P. Singh and D. Joseph, Fluid dynamics of floating particles, J. Fluid Mech. **530**, 31 (1999).
[28] J. Lucassen, Capillary forces between solid particles in fluid interfaces, Colloids Surf. **65**, 131 (1992).
[29] S. Timoshenko and J. Gere, *Theory of Elastic Stability* (McGraw-Hill, New York, 1961).
[30] N. Taccoen, F. Lequeux, D. Z. Gunes, and C. N. Baroud, Probing the mechanical strength of an armored bubble and its implication to particle-stabilized foams, Phys. Rev. X **6**, 011010 (2016).
[31] P. Kralchevsky, I. Ivanov, K. Ananthapadmanabhan, and A. Lips, On the thermodynamics of particle-stabilized emulsions: Curvature effects and catastrophic phase inversion, Langmuir **21**, 50 (2005).
[32] P. Cicuta and D. Vella, Granular character of particle rafts, Phys. Rev. Lett. **102**, 138302 (2009).
[33] O. Saavedra V., H. Elettro, and F. Melo, Progressive friction mobilization and enhanced Janssen's screening in confined granular rafts, Phys. Rev. Mater. **2**, 043603 (2018).
[34] B. Andreotti, Y. Forterre, and O. Pouliquen, *Granular Media: Between Fluid and Solid* (Cambridge University Press, Cambridge, 2013).
[35] D. Vella, A. Boudaoud, and M. Adda-Bedia, Statics and inertial dynamics of a ruck in a rug, Phys. Rev. Lett. **103**, 174301 (2009).
[36] I. Jorjadze, L.-L. Pontani, and J. Brujic, Microscopic approach to the nonlinear elasticity of compressed emulsions, Phys. Rev. Lett. **110**, 048302 (2013).
[37] T. S. Majmudar and R. P. Behringer, Contact force measurements and stress-induced anisotropy in granular materials, Nature (London) **435**, 1079 (2005).
[38] D. M. Mueth, H. M. Jaeger, and S. R. Nagel, Force distribution in a granular medium, Phys. Rev. E **57**, 3164 (1998).
[39] R. P. Behringer and B. Chakraborty, The physics of jamming for granular materials: A review, Rep. Prog. Phys. **82**, 012601 (2019).
[40] J. F. Peters, M. Muthuswamy, J. Wibowo, and A. Tordesillas, Characterization of force chains in granular material, Phys. Rev. E **72**, 041307 (2005).
[41] D. M. Goggin, R. Bei, R. Anderson, D. A. Gómez-Gualdrón, and J. R. Samaniuk, Stacking of monolayer graphene particles at a water–vapor interface, J. Phys. Chem. C **125**, 7880 (2021).
[42] S. Gravelle and L. Botto, Adsorption of single and multiple graphene-oxide nanoparticles at a water–vapor interface, Langmuir **37**, 13322 (2021).
[43] J. E. Jones, On the determination of molecular fields. II. From the equation of state of a gas, Proc. R. Soc. London A **106**, 463 (1924).
[44] A. Lerf, A. Buchsteiner, J. Pieper, S. Schöttl, I. Dekany, T. Szabo, and H. Boehm, Hydration behavior and dynamics of water molecules in graphite oxide, J. Phys. Chem. Solids **67**, 1106 (2006).
[45] T. Dyer, N. Thamwattana, and R. Jalili, Modelling the interaction of graphene oxide using an atomistic-continuum model, RSC Adv. **5**, 77062 (2015).
[46] R. A. Soler-Crespo, W. Gao, L. Mao, H. T. Nguyen, M. R. Roenbeck, J. T. Paci, J. Huang, S. T. Nguyen, and H. D. Espinosa, The role of water in mediating interfacial adhesion and shear strength in graphene oxide, ACS Nano **12**, 6089 (2018).
[47] C.-h. Liu, S. R. Nagel, D. Schecter, S. Coppersmith, S. Majumdar, O. Narayan, and T. Witten, Force fluctuations in bead packs, Science **269**, 513 (1995).
[48] S. N. Coppersmith, C.-h. Liu, S. Majumdar, O. Narayan, and T. A. Witten, Model for force fluctuations in bead packs, Phys. Rev. E **53**, 4673 (1996).
[49] M. Cavallaro Jr., L. Botto, E. P. Lewandowski, M. Wang, and K. J. Stebe, Curvature-driven capillary migration and assembly of rod-like particles, Proc. Natl. Acad. Sci. USA **108**, 20923 (2011).
[50] T. Carey, O. Cassidy, K. Synnatschke, E. Caffrey, J. Garcia, S. Liu, H. Kaur, A. G. Kelly, J. Munuera, C. Gabbett *et al.*, High-mobility flexible transistors with low-temperature solution-processed tungsten dichalcogenides, ACS Nano **17**, 2912 (2023).
[51] J. Kim, L. J. Cote, F. Kim, W. Yuan, K. R. Shull, and J. Huang, Graphene oxide sheets at interfaces, J. Am. Chem. Soc. **132**, 8180 (2010).
[52] Y. Chen, F. Guo, A. Jachak, S.-P. Kim, D. Datta, J. Liu, I. Kulaots, C. Vaslet, H. D. Jang, J. Huang *et al.*, Aerosol synthesis of cargo-filled graphene nanosacks, Nano Lett. **12**, 1996 (2012).
[53] C.-J. Shih, S. Lin, M. S. Strano, and D. Blankschtein, Understanding the stabilization of liquid-phase-exfoliated graphene in polar solvents: Molecular dynamics simulations and kinetic theory of colloid aggregation, J. Am. Chem. Soc. **132**, 14638 (2010).
[54] A. Agrawal, S. Gravelle, C. Kamal, and L. Botto, Viscous peeling of a nanosheet, Soft Matter **18**, 3967 (2022).
[55] J. M. Stockie and S. I. Green, Simulating the motion of flexible pulp fibres using the immersed boundary method, J. Comput. Phys. **147**, 147 (1998).